Electronic Supplementary Material (ESI) for Journal of Materials Chemistry A.

Modulating the localized electronic distribution of Cu species during reconstruction for enhanced electrochemical CO_2 reduction to C_{2+} products

Zongmiao Li,[‡ab] Zhu Liu,[‡b] Shiju Li,[a] Yuhou Pei,[ab] Di Li,[ab] Jiale Mao,[ab] Rong Zhou,[c] Chuntian Qiu,[b] Yingying Lu,[*ab] and Bing Zhang[*ab]

[a] State Key Laboratory of Chemical Engineering, College of Chemical and Biological Engineering, Institute of Pharmaceutical Engineering, Zhejiang University, Hangzhou, 310027, P. R. China. E-mail: bzhang219@zju.edu.cn, yingyinglu@zju.edu.cn.

[b] ZJU-Hangzhou Global Scientific and Technological Innovation Center, Zhejiang University, Hangzhou, 311215, P.R. China.

[c] College of Chemistry and Chemical Engineering, Xinjiang Agricultural University, Urumqi, 830052, China.

‡ These authors contributed equally.

.

Table of contents

Faradaic efficiency calculation

All electrochemical measurements were run at 25 °C in a home-made flow cell with a typical three-electrode configuration: CuO-ZrO_2-x coated GDE, platinum foil, saturated Ag/AgCl were used as the working electrode, counter electrode and reference electrode, respectively. The anion exchange membrane was used to separate the anolyte and catholyte chamber both filled with 1 M KOH. A CHI660E electrochemical workstation was employed to record the electrochemical response. All potentials measured against Ag/AgCl were converted to the RHE (reversible hydrogen electrode) in this work according equation E(vs. RHE)= E (vs. Ag/AgCl) + 0.199V + 0.059 × pH - 0.85iR, where R was measured by electrochemical impedance spectroscopy (EIS). During the electrochemical tests, the flow rate of CO_2 was 25 sccm, and the electrolyte flow rates for cathode and anode were 15 mL min^{-1} and 20 mL min^{-1} respectively. The gaseous products of CO_2RR were quantified by online gas chromatograph and the liquid products were analyzed by the 1H NMR spectroscopy, where DMSO and D_2O were used as the reference standard and the deuterated solvent. The Faradaic efficiency (FE) of gas product was calculated by the following equation:

$$FE_g = x_i \times v \times \frac{n_i F P}{RT} \times \frac{1}{j_{total}} \times 100\%$$

where x_i is the volume fraction of gas product determined by online GC referenced to the calibrated standard product, v is the gas flow rate, n_i is the number of electrons required to produce one molecule of product i, F is the Faraday constant (96485 C mol^{-1}), P is the atmosphere pressure, R is the ideal gas constant, T is the temperature, and j_{total} is the total current.

The FE of liquid products was calculated by the following equation:

$$FE_{liquid} = y_i \times \frac{n_i F}{Q} \times 100\%$$

where y_i is the moles of product i, Q is the cumulative charge as the liquid products collected.

Density functional theory calculations

Spin-polarized density functional theory (DFT) calculations were conducted with the Vienna ab initio Simulation Program (VASP),[1-2] using the Perdew-Burke-Ernzerhof (PBE) functional[3] within the generalized gradient approximation, along with the projected augmented wave (PAW) pseudopotentials[4] to treat the exchange-correlation energy interactions among electrons. In order to simulate the adsorption of intermediates on the modelling system, the suggested oriented crystallographic facet (110) of Cu_2O cubical phase from the TEM and XRD characterization was adopted to generate the interface between Cu_2O and ZrO_2 by doping a Zr atom into the Cu_2O (110) slab, as shown in Figure S19. To vary the tendency of the oxidation state of the surface Cu in contact with ZrO_2, the Bader charges analysis was performed given that the Bader charge qualitatively corresponds to the oxidation state, which is shown in Figure

4f in the main text. The amount of charge transfer from Cu to Zr atoms is computed by Bader charge analysis according to the equation:

$$Q_{Cu} = Z_{Cu} - q_{Bader},$$

where Z and q represent the number of valence electrons and the values of Bader charges of the Cu atom.[5-6]

The modelling system, as shown in Figure S19, was constructed by a four-layer slab with a vacuum region of 20 Å along the z-axis to minimize the periodic image interactions. An energy cutoff was set to 450 eV to expand the wave functions. Brillouin zone integration was sampled with 2 × 4 × 1 Monkhorst-Pack mesh k-points grids[7] for geometry optimizations and 10 × 20 × 1 k-points grids for electronic property calculations, respectively. All geometries were fully optimized until the convergence criteria of forces and energies reach 0.015 eV/ Å for the forces and 1×10^{-4} eV for the energies on all atoms. The slab-to-slab dipole corrections were included in the perpendicular direction along the surface of the slab model.[8-9] The adsorption energies (E_{ad}) of intermediates on the Cu_2O-ZrO_2 surface are estimated according to the following equation:

$$E_{ad} = E_{surf + im} - E_{surf} - E_{im},$$

where $E_{surf + im}$ represents the total energy of the intermediates adsorbed on the surface, E_{surf} is the energy of the Cu_2O-ZrO_2 (110) surface and E_{im} is the energy of the respective isolated intermediate. The free energy of the adsorbed state is carried out as follows:

$$\Delta G_{*im} = \Delta E_{*im} + \Delta E_{ZPE} - T\Delta S,$$

where ΔE_{ZPE} is the difference corresponding to the zero point energy and ΔS is the entropy.

Results

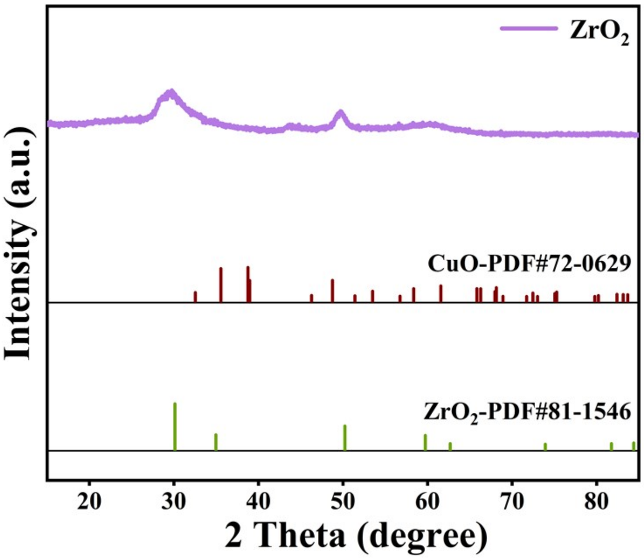

Supplementary Figure 1. XRD pattern of as-prepared ZrO_2

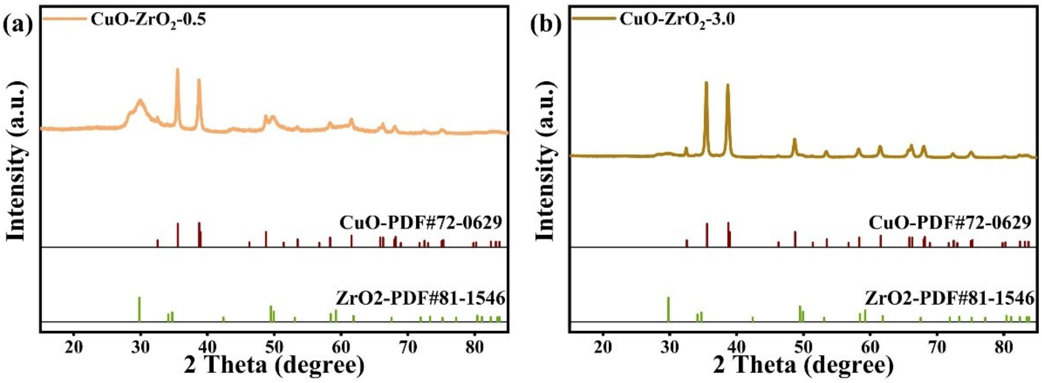

Supplementary Figure 2. XRD patterns of as-prepared CuO-ZrO$_2$-0.5 (a) and CuO-ZrO$_2$-3.0 (b).

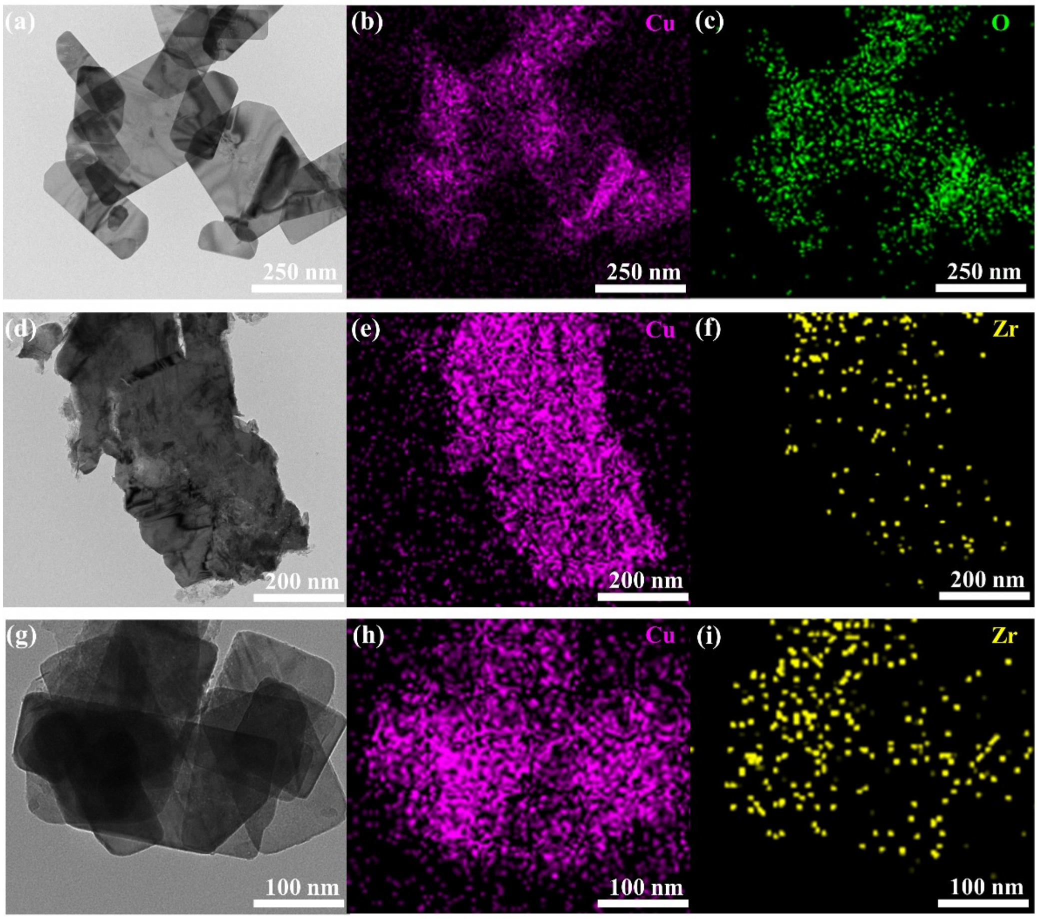

Supplementary Figure 3. The TEM images and corresponding EDS elemental mapping images of CuO (a, b and c), CuO-ZrO_2-0.5 (d, e and f) and CuO-ZrO_2-3.0 (g, h and i).

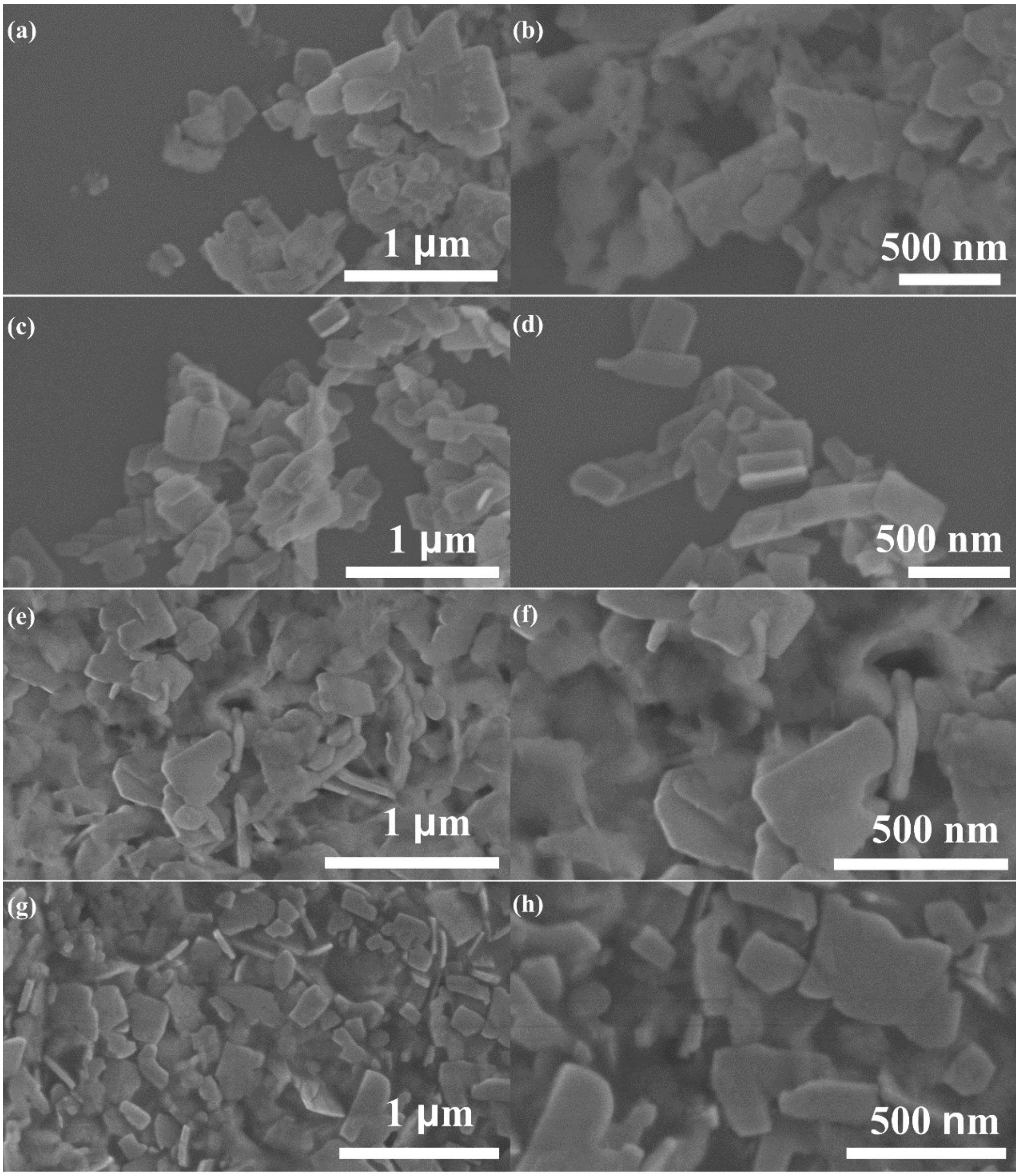

Supplementary Figure 4. The SEM images of CuO-ZrO_2-1.0 (a, b), CuO (c, d), CuO-ZrO_2-0.5 (e, f) and CuO-ZrO_2-3.0 (g, h).

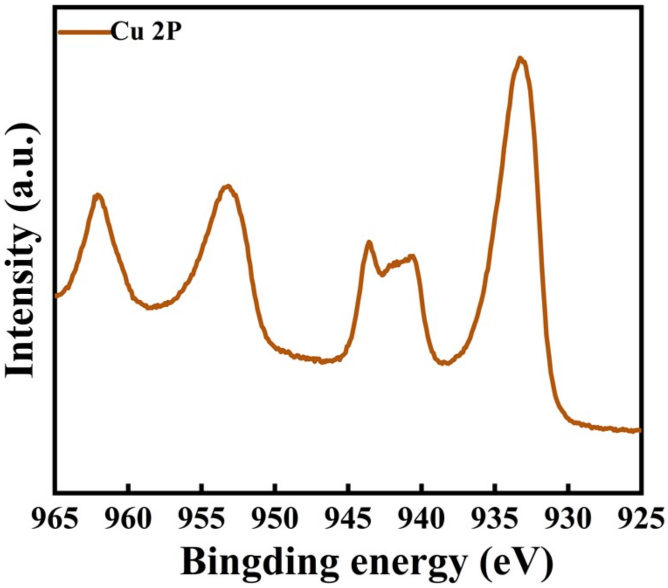

Supplementary Figure 5. Cu 2p XPS spectrum of CuO.

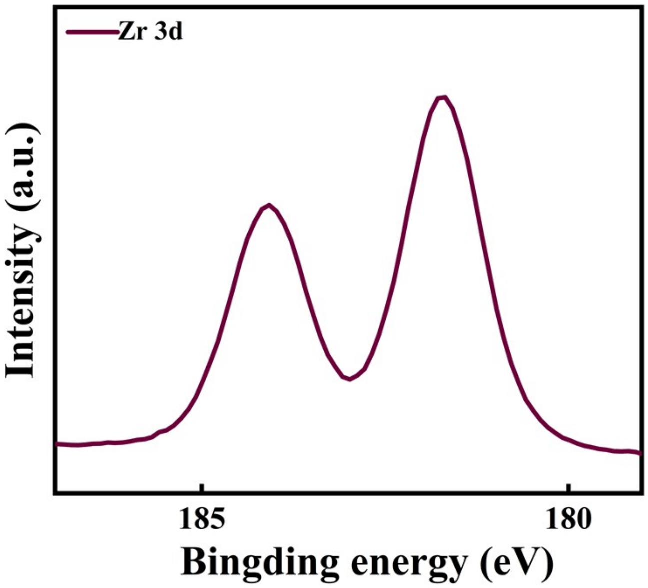

Supplementary Figure 6. Zr 3d XPS spectrum of ZrO_2.

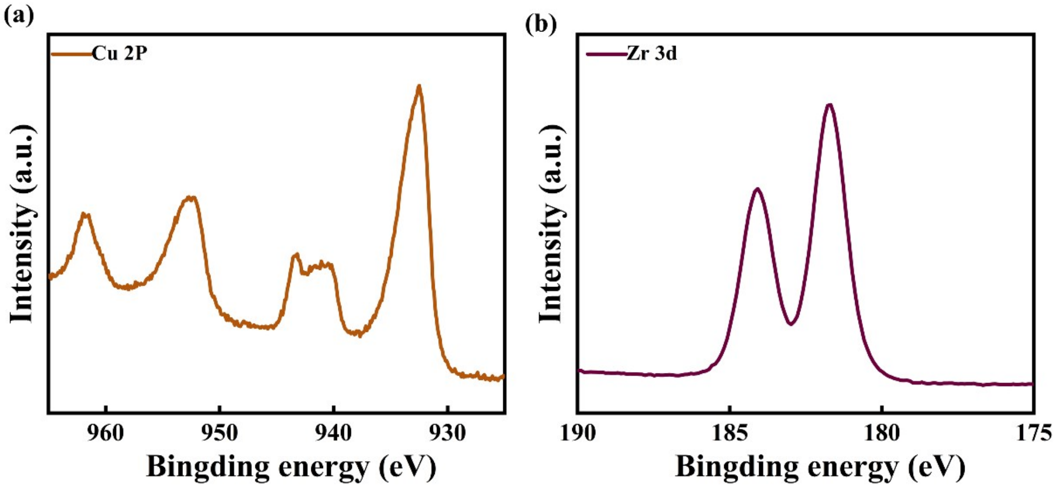

Supplementary Figure 7. Cu 2p (a) and Zr 3d (b) XPS spectra of CuO-ZrO_2-0.5.

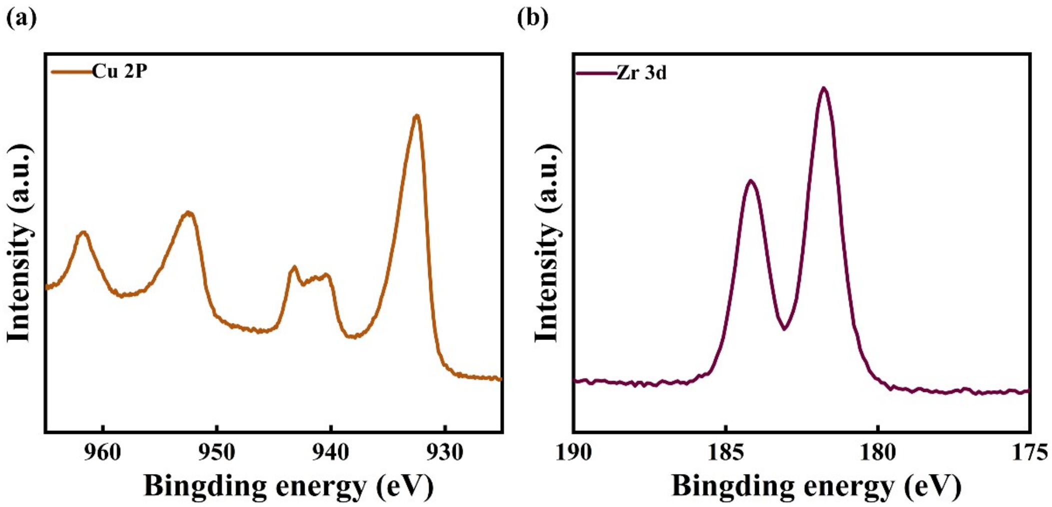

Supplementary Figure 8. Cu 2p (a) and Zr 3d (b) XPS spectra of CuO-ZrO_2-3.0.

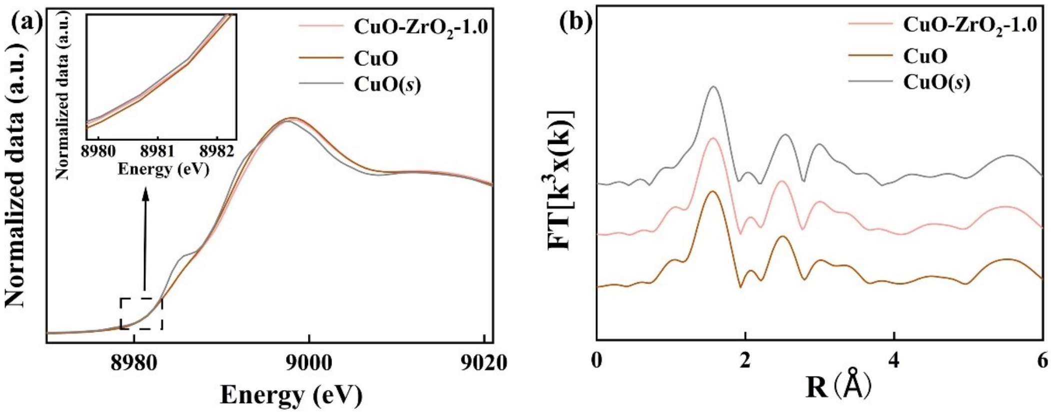

Supplementary Figure 9. Normalized Cu K-edge XANES spectra (a) and Fourier transforms of Cu K-edge EXAFS spectra (b) for CuO-ZrO_2-1.0 and CuO. Commercialized CuO nanoparticles were included as reference.

Supplementary Table S1. Normalized atomic proportion of CuO-ZrO_2 and CuO measured by XPS spectroscopy.

Catalyst	Normalized atomic proportion		
	Cu	Zr	O
CuO-ZrO_2-3.0	33.81	5.81	60.38
CuO-ZrO_2-1.0	19.94	11.28	68.78
CuO-ZrO_2-0.5	14.68	14.29	71.03
CuO	47.09	0	52.91

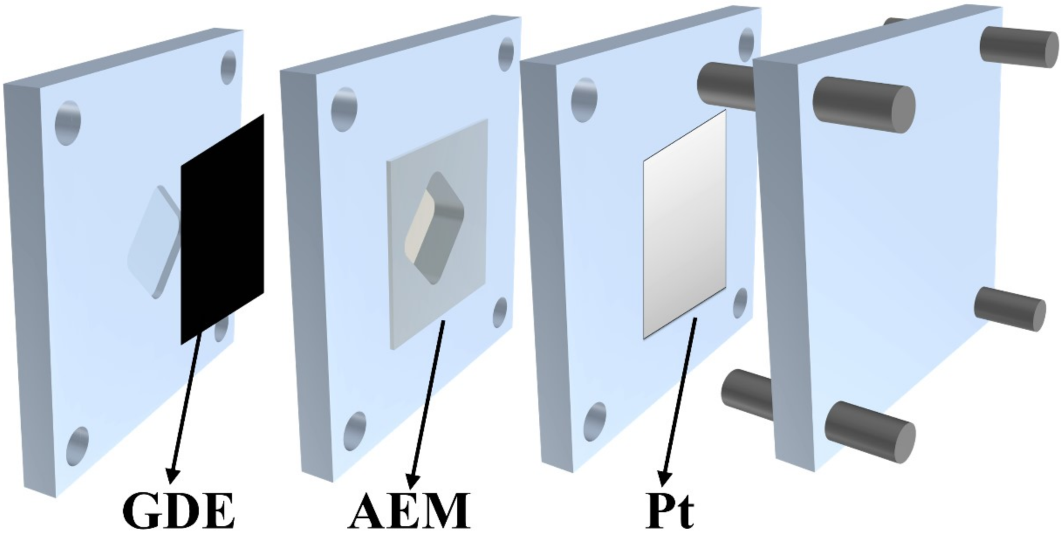

Supplementary Figure 10. The Schematic illustration for the flow cell.

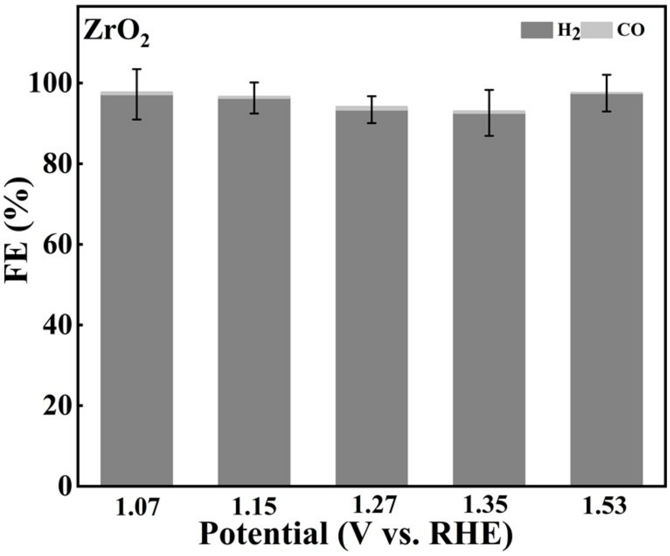

Supplementary Figure 11. The CO$_2$RR products distribution over ZrO$_2$ at different bias potentials.

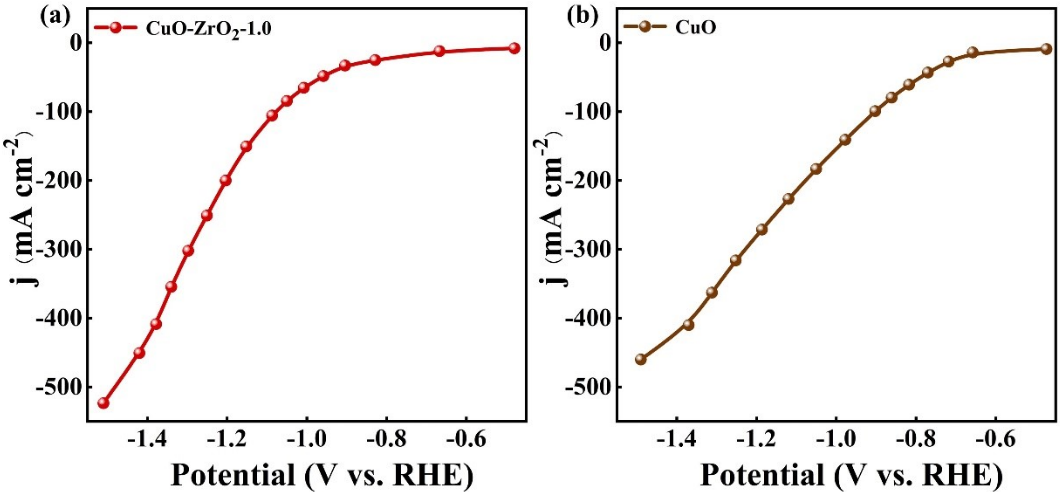

Supplementary Figure 12. The LSV curves of CuO-ZrO_2-1.0 (a) and CuO (b).

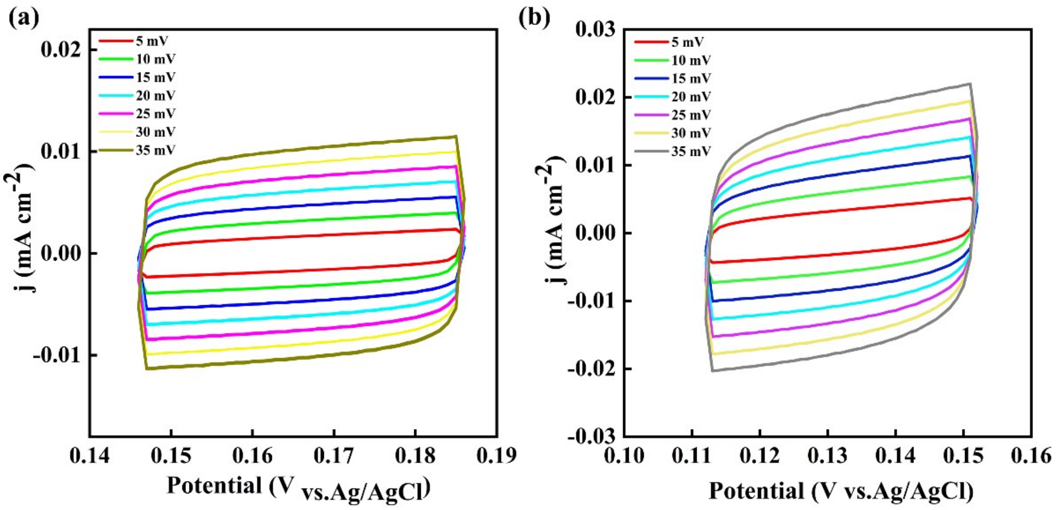

Supplementary Figure 13. CV curves ofCuO-ZrO_2-1.0 (a) and CuO (b).

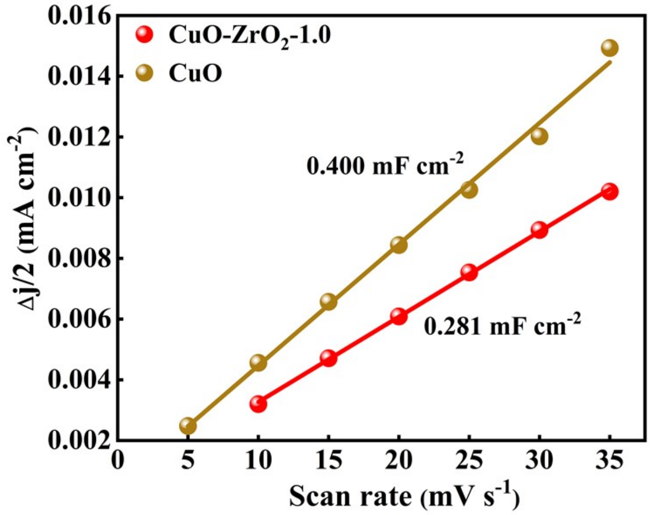

Supplementary Figure 14. Electrochemical double-layer capacitances of CuO-ZrO_2-1.0 and CuO.

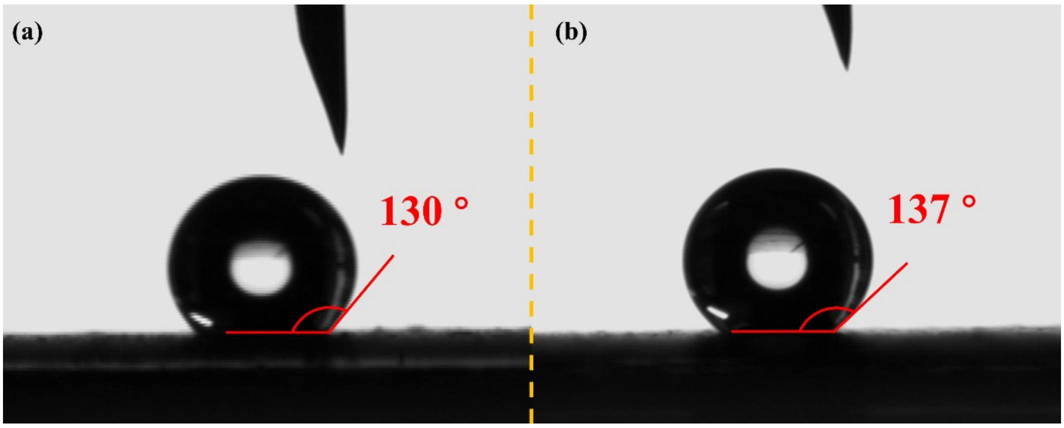

Supplementary Figure 15. Contact angle tests of CuO-ZrO$_2$-1.0 (a) and pristine CuO (b).

Supplementary Table S2. Summarized CO_2RR performances for C_{2+} products over various electrocatalysts.

Catalyst	Maximum C_{2+} FE (%)	Enhancement ratio of C_{2+} at Maximum FE	Ref.
CuO-ZrO_2-1	82.4	1.73	This work
SCO-B	59.1	1.68	[10]
Cu-12.5 nm	65.7	1.70	[11]
5-Ag/Cu_2O	65.0	1.18	[12]
CuNNAs	59.0	1.5	[13]
Cu-nr/CC3	76.1	1.17	[14]
M-Cu_1/Cu_{Np}	75.4	1.67	[15]
Cu-poly	71.08	1.15	[16]

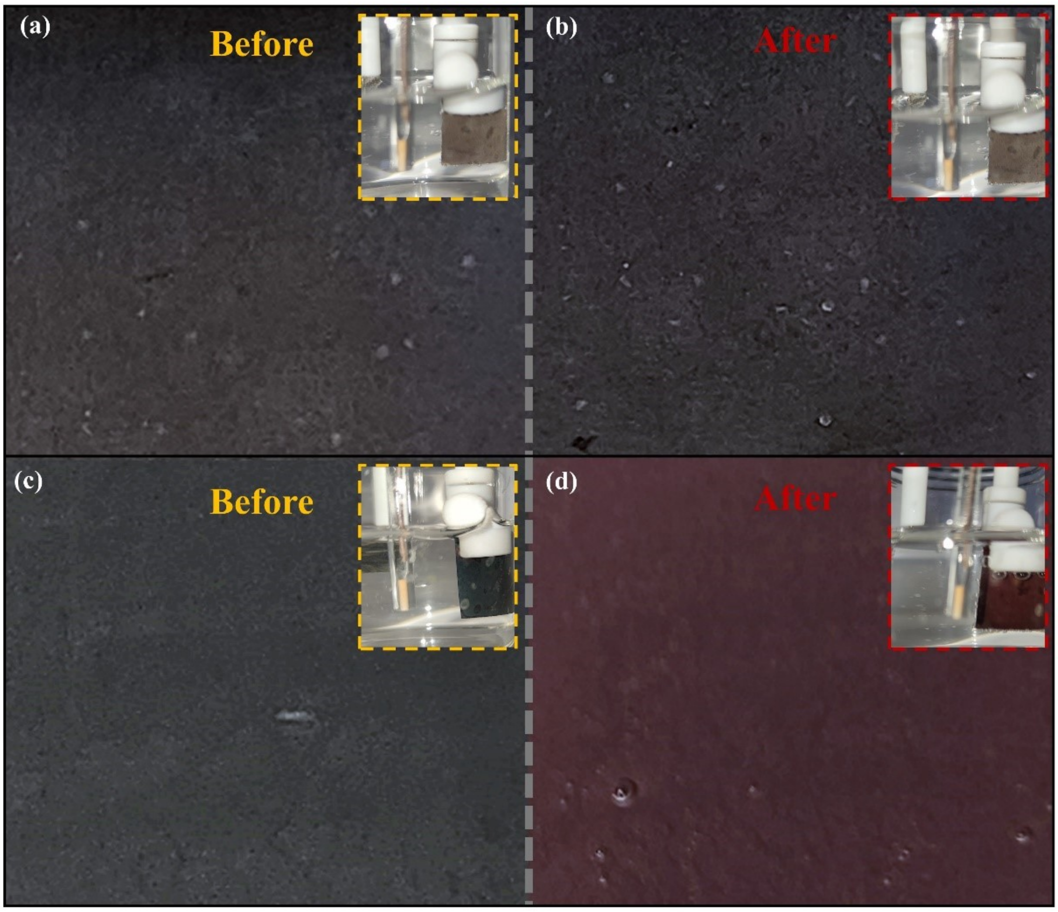

Supplementary Figure 16. The photographs of CuO-ZrO_2-1.0 (a, b) and CuO (c, d) on gas diffusion electrode before and after CO_2RR.

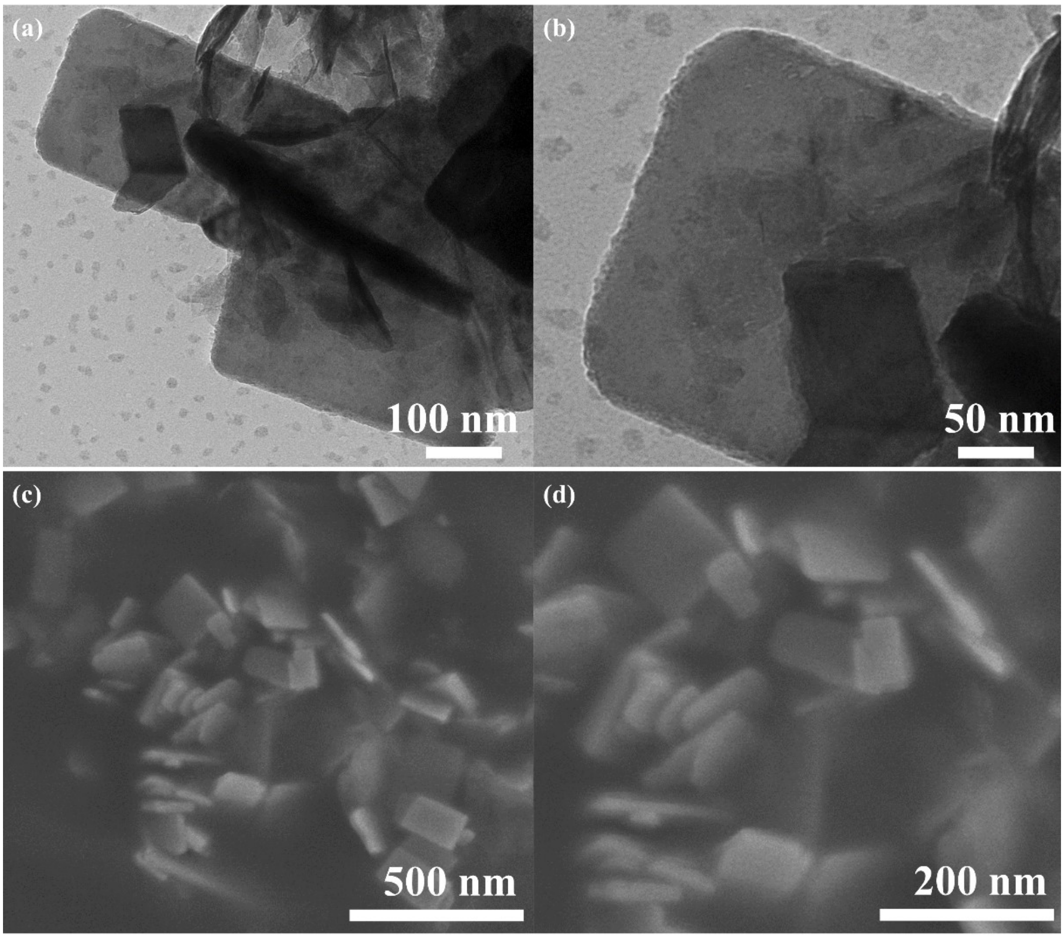

Supplementary Figure 17. The TEM (a, b) and SEM (c, d) images of CuO-ZrO_2-1.0 after CO_2RR (100 mA cm-2 for 20 min).

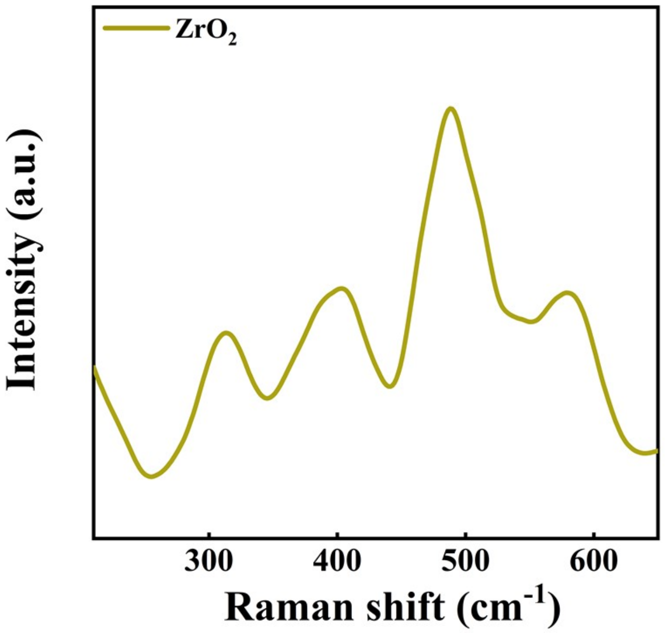

Supplementary Figure 18. The Raman spectrum of ZrO_2 in air.

Supplementary Table S3. Peak area of Cu^+/Cu^0 over $CuO\text{-}ZrO_2$-1 and CuO after reaction.

Catalyst	Peak area of Cu^+ (a. u.)	Peak area of Cu^0	The peak area ratio of Cu^+ to Cu^0
$CuO\text{-}ZrO_2$-1	51064	31713	1.73
CuO	32440	54077	0.60

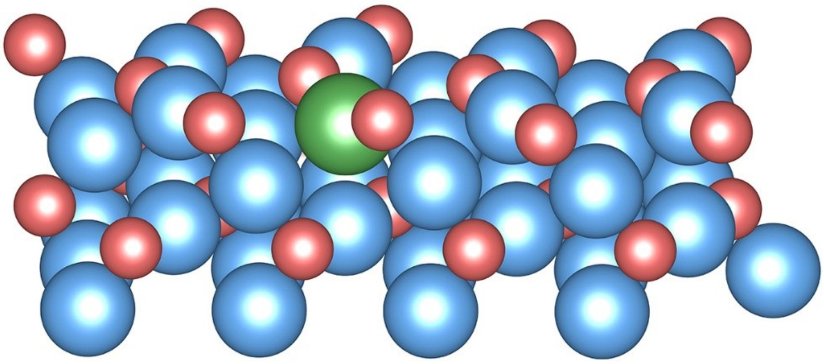

Supplementary Figure 19. The side view of the Cu_2O-ZrO_2 surface of the modeling slab. The balls in blue, red, and green stand for Cu, O, and Zr, respectively.

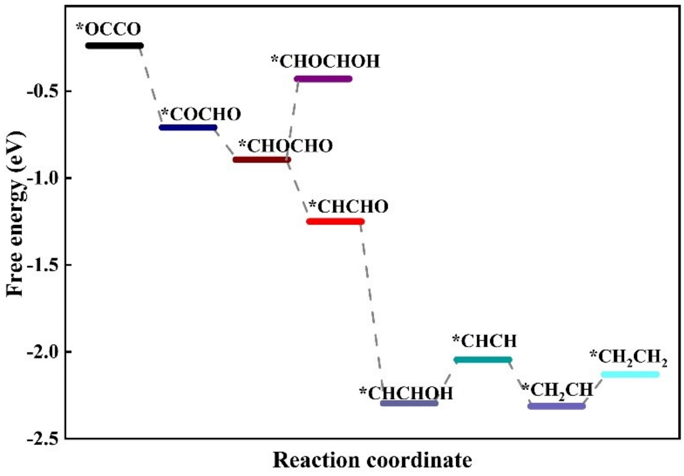

Supplementary Figure 20. Other C_2H_4 pathways over the Cu_2O-ZrO_2.

Supporting references

[1] G. Kresse, J. Furthmuller, *Comput. Mater. Sci.*, 1996, **6**, 15–50.

[2] G. Kresse, J. Furthmuller, *Phys. Rev. B*, 1996, **54**, 11169–11186.

[3] J. P. Perdew, K. Burke, M. Ernzerhof, *Phys. Rev. Lett.*, 1996, **77**, 3865–3868.

[4] P. E. Blöchl, *Phys. Rev. B*, 1994, **50**, 17953-17979.

[5] M. Yu, D. R. Trinkle, *J. Chem. Phys.*, 2011, **134**, 064111.

[6] E. Sanville, S. D. Kenny, R. Smith, G. Henkelman, *J. Comput. Chem.*, 2007, **28**, 899-908.

[7] H. J. Monkhorst, J. D. Pack, *Phys. Rev. B*, 1976, **13**, 5188-5192.

[8] G. Makov, M. C. Payne, *Phys. Rev. B*, 1995, **51**, 4014-4022.

[9] J. Neugebauer, M. Scheffler, *Phys. Rev. B*, 1992, **46**, 16067-16080.

[10] X. K. Lu, B. Lu, H. Li, K. Lim, L. C. Seitz, *ACS Catal.*, 2022, **12**, 6663-6671.

[11] Z. Chen, Y. Song, Z. Zhang, Y. Cai, H. Liu, W. Xie, D. Deng, *J. Energy Chem.*, 2022, **74**, 198-202.

[12] A. Herzog, A. Bergmann, H. S. Jeon, J. Timoshenko, S. Kühl, C. Rettenmaier, M. Lopez Luna, F. T. Haase, B. Roldan Cuenya, *Angew. Chem. Int. Ed.*, 2021, **60**, 7426-7435.

[13] Y. Zhou, Y. Liang, J. Fu, K. Liu, Q. Chen, X. Wang, H. Li, L. Zhu, J. Hu, H. Pan, M. Miyauchi, L. Jiang, E. Cortés, M. Liu, *Nano Lett.*, 2022, **22**, 1963-1970.

[14] C. Chen, X. Yan, Y. Wu, S. Liu, X. Zhang, X. Sun, Q. Zhu, H. Wu, B. Han, *Angew. Chem. Int. Ed.*, 2022, **61**, e202202607.

[15] J. Feng, L. Zhang, S. Liu, L. Xu, X. Ma, X. Tan, L. Wu, Q. Qian, T. Wu, J. Zhang, X. Sun, B. Han, *Nat. Commun.*, 2023, **14**, 4615.

[16] T. Zhao, X. Zong, J. Liu, J. Chen, K. Xu, X. Wang, X. Chen, W. Yang, F. Liu, M. Yu, F. Cheng, *Appl. Catal., B,* 2024, **340**, 123281.